



A 100 au Wide Bipolar Rotating Shell Emanating from the HH 212 Protostellar Disk: A Disk Wind?

Chin-Fei Lee^{1,2} , Zhi-Yun Li³, Claudio Codella⁴ , Paul T. P. Ho¹, Linda Podio⁴, Naomi Hirano¹, Hsien Shang¹ ,
Neal J. Turner⁵ , and Qizhou Zhang⁶

¹ Academia Sinica Institute of Astronomy and Astrophysics, P.O. Box 23-141, Taipei 106, Taiwan; cflee@asiaa.sinica.edu.tw

² Graduate Institute of Astronomy and Astrophysics, National Taiwan University, No. 1, Sec. 4, Roosevelt Road, Taipei 10617, Taiwan

³ Astronomy Department, University of Virginia, Charlottesville, VA 22904, USA

⁴ INAF, Osservatorio Astrofisico di Arcetri, Largo E. Fermi 5, I-50125 Firenze, Italy

⁵ Jet Propulsion Laboratory, California Institute of Technology, Pasadena, CA 91109, USA

⁶ Harvard-Smithsonian Center for Astrophysics, 60 Garden Street, Cambridge, MA 02138, USA

Received 2017 October 5; revised 2018 February 5; accepted 2018 February 7; published 2018 March 20

Abstract

HH 212 is a Class 0 protostellar system found to host a “hamburger”-shaped dusty disk with a rotating disk atmosphere and a collimated SiO jet at a distance of ~ 400 pc. Recently, a compact rotating outflow has been detected in SO and SO₂ toward the center along the jet axis at ~ 52 au ($0''.13$) resolution. Here we resolve the compact outflow into a small-scale wide-opening rotating outflow shell and a collimated jet, with the observations in the same S-bearing molecules at ~ 16 au ($0''.04$) resolution. The collimated jet is aligned with the SiO jet, tracing the shock interactions in the jet. The wide-opening outflow shell is seen extending out from the inner disk around the SiO jet and has a width of ~ 100 au. It is not only expanding away from the center, but also rotating around the jet axis. The specific angular momentum of the outflow shell is ~ 40 au km s⁻¹. Simple modeling of the observed kinematics suggests that the rotating outflow shell can trace either a disk wind or disk material pushed away by an unseen wind from the inner disk or protostar. We also resolve the disk atmosphere in the same S-bearing molecules, confirming the Keplerian rotation there.

Key words: accretion, accretion disks – ISM: individual objects (HH 212) – ISM: jets and outflows – stars: formation

1. Introduction

The HH 212 protostellar system is a well-studied young star-forming system located in Orion at a distance of ~ 400 pc. The central source is the Class 0 protostar IRAS 05413-0104 (Zinnecker et al. 1992). Previous Atacama Large Millimeter/submillimeter Array (ALMA) observations at high angular resolution at the wavelength of $850 \mu\text{m}$ have detected a vertically resolved dusty disk feeding the central protostar (Lee et al. 2017b). The disk is deeply embedded in an infalling-rotating envelope (Lee et al. 2017c). It has an atmosphere that shows a rotation motion around the central star. Detailed modeling to the kinematics of both the envelope and disk atmosphere indicates that the disk is rotating with a Keplerian rotation within ~ 40 au of the central star. A spinning jet is also detected, with an inferred launching radius on the disk of ~ 0.05 au from the central protostar (Lee et al. 2017a). It can carry away angular momentum from the innermost disk, allowing the material there to fall onto the central protostar.

Inside the disk itself, material is expected to be transported from the outer part to the inner part. Thus there must be a mechanism to remove the angular momentum from the material in the disk region outside the jet-launching region as well. This may be achieved with, e.g., magneto-rotational instability (Balbus & Hawley 2006) and low-velocity extended tenuous disk wind (Konigl & Pudritz 2000). Previous CH₃OH observations at ~ 240 au resolution suggested the presence of a disk wind component in HH 212 ejected from the disk at a radius of ~ 1 au (Leurini et al. 2016), surrounding the SiO jet. However, our new observations at ~ 16 au resolution show that CH₃OH actually traces the disk atmosphere within a radius of ~ 40 au of the center (Lee et al. 2017c). Nonetheless, disk wind

has also been suggested in other objects, e.g., CB 26 (Launhardt et al. 2009), DG Tau (Agra-Amboage et al. 2011), Orion BN/KL Source I (Greenhill et al. 2013; Hirota et al. 2017), and TMC1A (Bjerkeli et al. 2016). All of these suggest the presence of a disk wind component extracting the angular momentum from the outer disk.

In this paper, we aim to determine whether a disk wind exists in HH 212 as well, using our new high-resolution molecular line data. In previous ALMA observations at ~ 200 au ($0''.5$) resolution, Podio et al. (2015) has detected a collimated outflow in SO and SO₂ extending out from the disk, inside the large-scale molecular outflow detected in C³⁴S (Codella et al. 2014). Recent follow-up observations at ~ 52 au ($0''.13$) resolution toward the base of the collimated outflow have detected a compact rotating outflow that may trace a disk wind (Tabone et al. 2017). Here, we zoom into the rotating outflow in the same S-bearing molecules with ALMA at ~ 16 au ($0''.04$) resolution, which is ~ 3 times higher than the previous observations. At this high resolution, we resolve the outflow into a small-scale wide-opening rotating outflow shell and a collimated jet aligned with the SiO jet. We also resolve the outflow kinematics and discuss whether the rotating outflow shell traces a disk wind or disk material pushed away by an unseen inner wind that originated closer to the protostar. In addition, we also resolve the disk atmosphere in the same S-bearing molecules, confirming the Keplerian rotation there. Notice that some previous searches of disk wind were done in CO (see, e.g., Launhardt et al. 2009; Bjerkeli et al. 2016). However, here in HH 212, CO emission is complicated, arising from both the collimated outflow and the large-scale molecular outflow, and suffering from missing flux around the systemic

Table 1
Observation Logs

Cycle	Date (YYYY MM DD)	Array Configuration	Number of Antennas	Time on target (minutes)	Baselines (meter)
3	2015 Nov 05	C36-7/8	45	44	78–16196
3	2015 Dec 03	C36-7/8	32	44	17–6344

Table 2
Correlator Setup for Cycle 3 Project

Spectral Window	Line or Continuum	Number of Channels	Central Frequency (GHz)	Bandwidth (MHz)	Channel Width (kHz)
0	SO $N_J = 8_9-7_8$	960	346.528	234.375	244.140
1	CO $J = 3-2$	960	345.796	234.375	244.140
2	H ¹³ CO ⁺ $J = 4-3$	960	346.998	234.375	244.140
3	SiO $J = 8-7$	960	347.330	234.375	244.140
4	HCO ⁺ $J = 4-3$	1920	356.735	468.750	244.140
5	Continuum	1920	357.994	1875.000	976.562

velocity. Therefore, a detailed analysis is needed to search for a disk wind in CO. As a result, we defer our report of CO observations to a future publication.

1.1. SO and SO₂ around Sun-like protostars

Sulfur is severely depleted in cold molecular clouds, with an abundance being three orders of magnitude less than the cosmic abundance (e.g., Tielke et al. 1994). On the other hand, S-bearing molecules are very abundant in almost all the components associated with the low-mass star-forming process, from dark clouds to protostellar envelopes and slow outflows, as well as hot corinos (van Dishoeck & Blake 1998). This is due to the release of sulfur from the dust mantles that can be caused by either evaporation when the dust is heated to temperatures higher than ~ 100 K (e.g., in the hot corinos or at the disk surface), or their erosion in shocks due to gas-grain (sputtering) or grain-grain collisions (shattering), see, e.g., Pineau des Forêts et al. (1993) and Guillet et al. (2011, and references therein). In this context, S-bearing species, and, in particular, those more abundant such as SO and SO₂ can be considered among the best tracers to image the high-density gas components involved in the process leading to the formation of a Sun-like star, namely, the high-velocity collimated jet (Lee et al. 2010; Podio et al. 2015), the accretion shock occurring at the envelope-disk interface (Sakai et al. 2014a, 2014b; Lee et al. 2016; Sakai et al. 2017), the outflow cavity walls, and possibly the disk surface directly illuminated and heated by the central protostar (this paper). The relative abundances of S-bearing molecules depend on the main S-compounds released from mantles, i.e., if S is released in an atomic and/or molecular form such as H₂S or OCS, a still hotly debated open question (Wakelam et al. 2004; Codella et al. 2005; Podio et al. 2014). In any case, SO₂ is expected to mainly form due to the reaction between SO and OH (e.g., Pineau des Forêts et al. 1993). Indeed, the SO₂/SO abundance ratio has been proposed to be an efficient chemical clock to date the gas (Charnley 1997; Hatchell et al. 1998). Unfortunately, Wakelam et al. (2004) and Codella et al. (2005) have shown that this abundance ratio is not very useful, because the SO and SO₂ abundances depend on the initial S-carrier on the grain mantles. In addition, both species may not be tracing the same portion of the gas.

Recent observations of SO in the inner 50 au around the L1527 protostar, located in Taurus, confirmed high SO abundances (up to 10^{-7}) associated with the dense ($\geq 10^{5-6} \text{ cm}^{-3}$) gas revealing the accretion shock at the envelope-disk interface (Sakai et al. 2014a, 2014b, 2016, 2017). On the other hand, before the present work, Podio et al. (2015) traced SO high-velocity emission associated with the HH 212, with very high abundances (up to 10^{-6}). In addition, the authors observed outflow-velocity emission close to the protostar, showing small-scale velocity gradients, indicating that it originates partly from the rotating disk, and partly from the base of the jet, opening the way to investigations at higher spatial scale. Also the SO abundances in the HH 212 jet have been estimated to be very high, up to 10^{-6} , confirming what was suggested by Lee et al. (2010) for the HH 211 protostellar jet. Also the SO₂ abundance has been measured to be $\sim 10^{-6}$. On the other hand, Podio et al. (2015) found in the HH 212 disk $X_{\text{SO}} = 10^{-8}-10^{-7}$, i.e., values higher by 3–4 orders of magnitude than those derived in protoplanetary disks (Fuente et al. 2010; Dutrey et al. 2011). These high abundances are plausibly due to either violent shocks caused by jets traveling, or slow shocks occurring close to the protostar, such as the accretion shocks already observed in HH 212 by Lee et al. (2017a).

2. Observations

Observations of the HH 212 protostellar system were carried out with ALMA in Band 7 at ~ 350 GHz in Cycle 3, with 32–45 antennas (see Table 1). Two executions were carried out in 2015, one on November 5 and the other on December 3. The projected baselines are 17–16196 m. The maximum recoverable size (MRS) scale is $\sim 0''.4$, enough to cover the compact outflow seen in SO and SO₂ near the central source (Tabone et al. 2017). One pointing was used to map the center of the system. The correlator was set up to have six spectral windows, with one for SO $N_J = 8_9-7_8$ at 346.528481 GHz, one for CO $J = 3-2$ at 345.795991 GHz, one for H¹³CO⁺ $J = 4-3$ at 346.998338 GHz, one for SiO $J = 8-7$ at 347.330631 GHz, one for HCO⁺ $J = 4-3$ at 356.734288 GHz, and one for the continuum at 358 GHz with many weak SO₂ lines (see Table 2). The total time on the HH 212 system is ~ 88 minutes.

Table 3
Calibrators and Their Flux Densities

Date (YYYY MM DD)	Bandpass Calibrator (Quasar, Flux Density)	Flux Calibrator (Quasar, Flux Density)	Phase Calibrator (Quasar, Flux Density)
2015 Nov 05	J0423–0120, 0.55 Jy	J0423–0120, 0.55 Jy	J0541–0211, 0.22 Jy
2015 Dec 03	J0510+1800, 4.07 Jy	J0423–0120, 0.67 Jy	J0541–0211, 0.23 Jy

Table 4
Line Properties from Splatalogue

Molecule	Frequency (GHz)	Transition QNs	$S_{ij}\mu^2$ (D ²)	$\log_{10}(A_{ij})$ (s ⁻¹)	E_{up} (K)	Linelist
SO	346.52848	9(8)–8(7)	21.52703	–3.26062	78.77510	JPL
SO ₂	356.75519	10(4, 6)–10(3, 7)	13.03465	–3.48408	89.83365	JPL
SO ₂	357.16536	13(4, 10)–13(3, 11)	17.87923	–3.45447	122.96459	JPL
SO ₂	357.24119	15(4, 12)–15(3, 13)	21.14165	–3.44140	149.68170	JPL
SO ₂	357.38757	11(4, 8)–11(3, 9)	14.64155	–3.47079	99.95222	JPL
SO ₂	357.58145	8(4, 4)–8(3, 5)	9.76046	–3.51492	72.36335	JPL
SO ₂	357.67178	9(4, 6)–9(3, 7)	11.40052	–3.49544	80.63686	JPL
SO ₂	357.89244	7(4, 4)–7(3, 5)	8.08092	–3.54144	65.01106	JPL
SO ₂	357.92596	6(4, 2)–6(3, 3)	6.34115	–3.58446	58.57965	JPL
SO ₂	357.96289	17(4, 14)–17(3, 15)	24.42371	–3.42881	180.11104	JPL
SO ₂	358.01309	5(4, 2)–5(3, 3)	4.49029	–3.66149	53.06831	JPL
SO ₂	358.03808	4(4, 0)–4(3, 1)	2.44211	–3.83876	48.47653	JPL
SO ₂	358.21564	20(0, 20)–19(1, 19)	44.65235	–3.23457	185.32964	JPL

The data were calibrated with the CASA package (version 4.5) for the passband, flux, and gain (see Table 3). In this paper, we only present the observational results in SO and SO₂ in order to search for a disk wind. The velocity resolution is $\sim 0.212 \text{ km s}^{-1}$ per channel for the lines in the spectral line windows and $\sim 0.848 \text{ km s}^{-1}$ per channel for the lines in the continuum window. In order to improve the signal-to-noise ratio in the spectral line windows, we binned four channels to make a bigger channel with a width of $\sim 0.848 \text{ km s}^{-1}$. We used a Briggs weighting with a robust factor of 0.5 for the visibility weighting to generate the SO and SO₂ channel maps at an angular resolution of $\sim 0''.04$ and a velocity resolution of $\Delta v_c = 0.848 \text{ km s}^{-1}$ per channel. In generating the SO and SO₂ maps, the data with the uv -distance greater than 12,000 m and 8000 m (with a corresponding angular scale of $\sim 0''.015$ and $0''.022$, respectively) are excluded, respectively, because no emission is detected there. Also an outer taper of $0''.03$ was used to obtain a better signal-to-noise ratio. The noise level can be measured from line-free channels. It is $\sim 1.85 \text{ mJy beam}^{-1}$ (or $\sim 12.4 \text{ K}$) for the SO channel maps. Twelve SO₂ lines are detected (see Table 4) and stacked, and the noise level is $\sim 0.48 \text{ mJy beam}^{-1}$ (or $\sim 3.0 \text{ K}$) for the resulting SO₂ channel maps. The velocities in the channel maps are LSR velocities. Various integrated maps are produced with various velocity ranges in order to show the low-velocity, high-velocity, and total integrated maps. The rms levels in those maps are estimated from the emission-free region in the same map or the emission-free integrated map with the same velocity width.

3. Results

For comparison, Figure 1(a) shows the previous maps of the dusty accretion disk in the $850 \mu\text{m}$ continuum (Lee et al. 2017b), the disk atmosphere in CH₂DOH (Lee et al. 2017c), and the collimated jet in SiO (Lee et al. 2017a). These maps have been rotated by 22.5° clockwise to align the jet axis in the north–south direction in order to facilitate our presentations.

The jet has a mean inclination angle of $\sim 4^\circ \pm 2^\circ$ to the plane of the sky, with the northern component tilted toward us (Claussen et al. 1998; Lee et al. 2007). The disk is perpendicular to the jet axis and nearly edge-on with the nearside tilted slightly by $\sim 4^\circ \pm 2^\circ$ to the south (Lee et al. 2017b). The atmosphere is better detected in the south than in the north. In the following, our maps of SO and SO₂ are presented together with the jet, disk, and disk atmosphere in order to show the connection to them. In this system, the systemic velocity is assumed to be $V_{\text{sys}} = 1.7 \pm 0.1 \text{ km s}^{-1}$ LSR (Lee et al. 2007), which is a mean value estimated before in CO $J = 1-0$ (Lee et al. 2000) and NH₃ (1, 1) (Wiseman et al. 2001). Figure 2 shows our SO and SO₂ spectra extracted from a rectangular region ($0''.4 \times 0''.2$ with the long side aligned with the jet axis) covering the emission from the central region. As can be seen, the systemic velocity lies roughly at the center of the spectra. Throughout this paper, in order to facilitate our presentations, we define an offset velocity $V_{\text{off}} = V_{\text{LSR}} - V_{\text{sys}}$. Also, velocities with $|V_{\text{off}}| \lesssim 3 \text{ km s}^{-1}$ are referred to as low and those outside the range as high. The low-velocity range is selected to show the disk atmosphere and a small-scale wide-opening outflow extending out from the inner disk, as discussed below.

3.1. SO Emission Morphology

A compact outflow has recently been detected in SO at $\sim 0''.13$ resolution, extending out from the central source along the jet axis (Tabone et al. 2017). Now at $\sim 0''.04$ resolution, we can resolve the outflow and check for a disk wind component. As shown in the total integrated emission map in Figure 1(b), the SO emission is detected here within $\sim \pm 0''.5$ of the central source around the SiO jet, extending out from the inner disk. The emission has a velocity with $|V_{\text{off}}| \lesssim 10 \text{ km s}^{-1}$. SO emission is also detected in the disk atmosphere, overlapping with the CH₂DOH emission. No SO emission is detected in the dusty disk, likely because the continuum emission is bright and

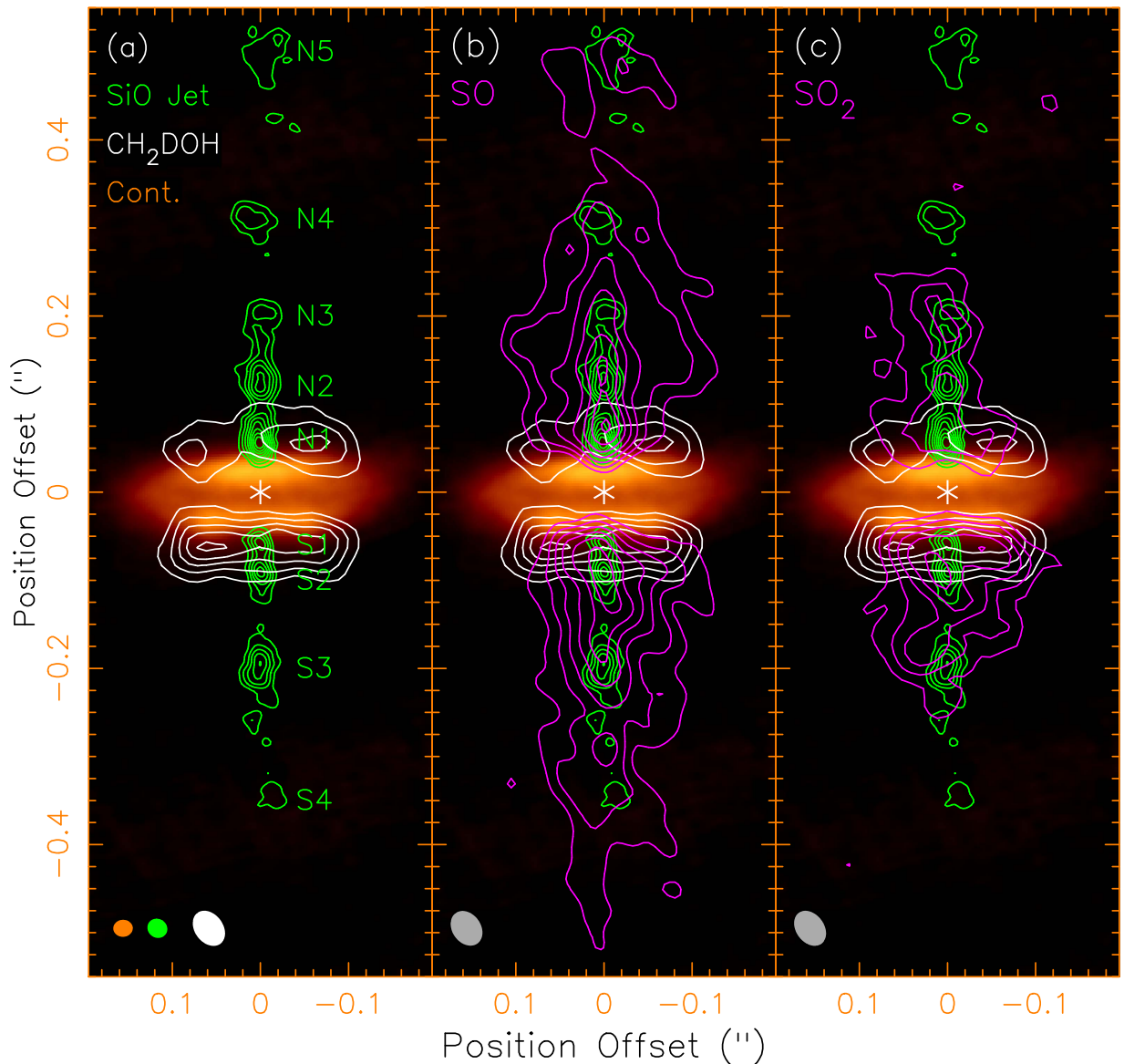


Figure 1. ALMA SO and SO₂ maps toward the center of the HH 212 system, on top of the dusty disk (orange image, from Lee et al. 2017b), the disk atmosphere (white contours, from Lee et al. 2017c), and the SiO jet (green contours, from Lee et al. 2017a). The maps are all rotated by 22°5 clockwise to align the jet axis in the north–south direction. The star marks the position of the central protostar. The magenta contours in (b) and (c) show the total integrated maps of SO ($V_{\text{off}} \sim -10.0$ to 10.0 km s^{-1}) and SO₂ ($V_{\text{off}} \sim -7.9$ to 6.5 km s^{-1}), respectively. The contours start at 3σ with a step of 2σ , where $\sigma = 0.009 \text{ Jy beam}^{-1} \text{ km s}^{-1}$ and $0.0022 \text{ Jy beam}^{-1} \text{ km s}^{-1}$ for SO and SO₂, respectively.

optically thick there (Lee et al. 2017c); thus, the emission behind it is blocked and the emission in front of it appears absorbed against the bright background.

Figure 3 shows the SO maps at low and high velocities. At low velocity, the outflow can be decomposed into two components, a wide-opening outflow extending out to $\sim 0''.2$ to the north and south from the inner disk, and a collimated jet along the jet axis (Figure 3(a)). The wide-opening outflow is reasonably resolved in the north, appearing as a shell structure opening out from the central source. The shell structure of the outflow can be better seen in the position–velocity (PV) diagrams as discussed below in Section 3.3. In the shell outside the atmosphere, the blueshifted emission overlaps with the redshifted emission (Figure 3(b)), indicating that the shell there is mainly radially expanding. At high velocity, the SO emission is seen around and along the jet axis (Figure 3(c)). As discussed later, since the projected velocity of the expanding shell can

reach up to V_{off} of $\pm 5 \text{ km s}^{-1}$, part of the emission traces the expanding shell projected on the jet axis. The emission peaks that spatially coincide with knots N3, N1, S1/S2, S3, and S4 should mainly trace the jet itself. Like the SiO jet, the blueshifted emission is seen more to the north and the redshifted emission is seen more to the south.

3.2. SO₂ Emission Morphology

A compact outflow has also been detected recently in SO₂ at $\sim 0''.13$ resolution (Tabone et al. 2017). Thus, we can also check for a disk wind component in SO₂. Here 12 SO₂ lines are detected (see Table 4) with $|V_{\text{off}}| \lesssim 8 \text{ km s}^{-1}$. They are weak and thus stacked to produce a mean SO₂ line with a better signal-to-noise ratio. As shown in the total integrated emission map in Figure 1(c), the SO₂ emission is detected within $\sim \pm 0''.3$ of the central source, not only tracing the outflow but also

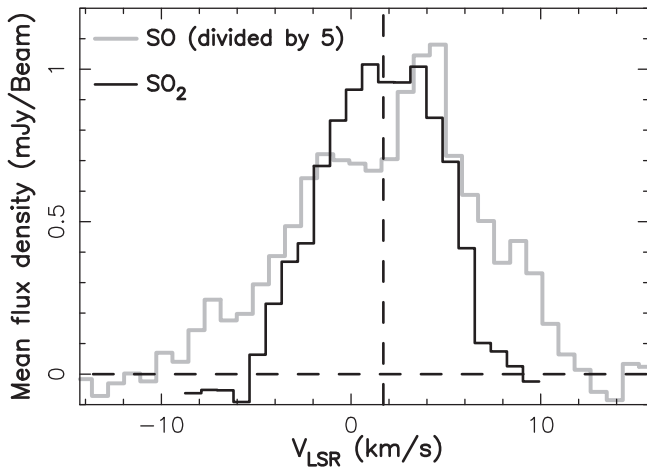


Figure 2. SO (gray curve) and SO₂ (black curve) spectra averaged over a rectangular region of $0''.4 \times 0''.2$ centered at the central source aligned with the jet axis. The SO flux density has been divided by 5 in order to be plotted with SO₂.

tracing the inner disk atmosphere. No SO₂ emission is detected toward the dusty disk because of the same reason as discussed above.

Figure 4 shows the SO₂ maps at low and high velocities. At low velocity, unlike the SO emission, the SO₂ emission traces mainly the inner disk atmosphere, as seen in Figures 4(a) and (b). The disk atmosphere is rotating with the redshifted emission in the east and blueshifted emission in the west, the same rotation sense as that found before in CH₃DOH, as indicated by the blue and red arrows in Figure 4(b). Like that seen in SO, the outflow in the north can also be decomposed into a wide-opening outflow and a collimated jet. In the north, the shell structure of the wide-opening outflow can be seen in the east. In the south, the shell structure can only be barely seen in the east, because it is contaminated by the emission around knot S3. At high velocity, like the SO emission, the SO₂ emission is mainly seen around the jet axis, with the blueshifted emission to the north and redshifted emission to the south (Figure 4(c)).

3.3. Kinematics

Figure 5 shows the position–velocity (PV) diagrams along the jet axis in SO and SO₂ in order to study the expansion velocity of the wide-opening outflow. The PV diagram of the SO₂ emission shows roughly a parabolic structure opening up from the source position to $\sim 0''.2$ to the north and south to $V_{\text{off}} \sim \pm 5 \text{ km s}^{-1}$, as guided by the white curves. The PV diagram of the SO emission is complicated. Part of the SO emission follows the parabolic structure seen in SO₂ and part of the SO emission is associated with the knots in the jet. The parabolic PV structure is associated with the wide-opening outflow, supporting that the wide-opening outflow is a shell and that the expansion velocity of the shell increases with the distance.

Figure 6 shows the intensity weighted velocity (first moment) maps of the SO and SO₂ emission at low velocities in order to search for the rotation in the shell. In SO, the eastern and western outer edges (as roughly delineated by the white curves) of the shell mostly have opposite velocities (Figure 6(a)), indicating that the shell is also rotating around the jet axis, in addition to the expansion mentioned above. The

rotation of the shell has the same sense as that of the disk, as indicated by the red and blue arrows. On the other hand, as discussed earlier, the SO₂ emission mainly arises from the rotating disk atmosphere (Figure 6(b)). The outflow edges are too faint in SO₂ to appear in this figure.

3.3.1. Rotation and Expansion in the Shell

Figure 7 shows the PV diagrams cut across the jet axis at increasing distance z from the disk midplane with a step of $0''.025$ (or 10 au) to the north and south, in order to study the expansion and rotation in the shell in detail. Since the kinematics in the northern part is better resolved than that in the southern part, our kinematic study here is based mainly on the northern part.

Near the bottom of the northern atmosphere at $z = 0''.05$, the PV diagram shows the redshifted emission in the east and blueshifted emission in the west (Figure 7(a)), as expected for a rotating disk atmosphere. In addition, the SO emission shows a velocity increasing toward the center, with the outer boundary of its PV structure well described by the Keplerian rotation velocity profile (magenta curves) due to the central protostar (Lee et al. 2017c). This confirms the presence of a rotationally supported disk orbiting the protostar. The mass of the protostar is $\sim 0.25 M_{\odot}$ from the kinematics of the disk and envelope in molecular lines (Lee et al. 2017c). At low velocities where the emission traces the outer part of the atmosphere, the PV structure can be roughly described by a tilted elliptical structure as guided by the green ellipse. This outer part is also seen in SO₂ emission. This PV structure confirms that the outer part of the atmosphere is not only rotating but also expanding (Hirota et al. 2017), indicating that the atmosphere there has become a part of the outflow shell. The upper part of the ellipse is much fainter than the lower part, probably because the emission in the nearside is self-absorbed. As we go higher up in the atmosphere to $z = 0''.075$, the elliptical PV structure becomes broader in the minor axis (Figure 7(b)), indicating that the expansion motion becomes faster higher up, consistent with the discussion above.

In the shell slightly above the disk atmosphere at $z = 0''.1$, the PV diagrams also show a tilted elliptical PV structure (green ellipse, Figure 7(c)), indicating that the shell there is also rotating and expanding. As compared to that seen in the atmosphere, it is broader in the minor axis, indicating that the expansion motion is faster. As we go further to the north to $z \geq 0''.125$, the PV structure can be decomposed into two components, one with an elliptical structure for the shell, and the other along the jet axis tracing the emission in the jet (Figures 7(d)–(g)). The major axis of the ellipse is almost aligned with the x -axis, indicating that the gas motion in the shell is dominated by the expansion. In addition, the SO₂ emission of the shell becomes very faint at low velocities, thus the limb-brightened shell (outflow edge) becomes faint and not detected, as seen in Figure 4(a). As a result, the emission of the shell is mainly detected at high velocities, appearing mainly around the jet axis, as seen in Figure 4(c).

In the southern part, similar elliptical PV structures can also be roughly seen for the shell in the atmosphere (Figures 7(h) and (i)). However, no clear elliptical PV structures can be identified easily (Figures 7(j)–(n)) in the PV diagrams above the disk atmosphere. Therefore, we will not attempt to fit the PV structures here because the results would be quite uncertain.

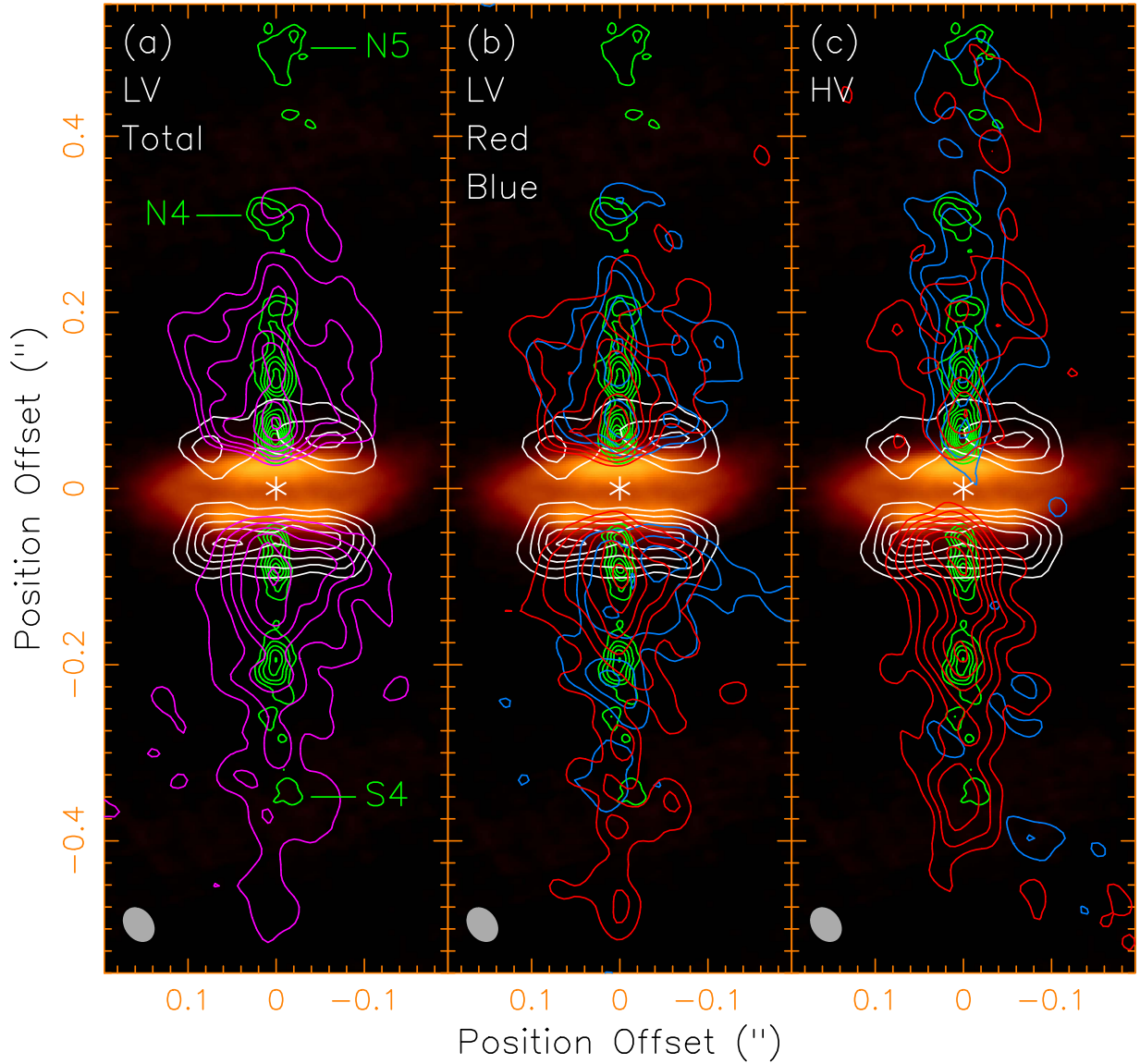


Figure 3. Low-velocity and high-velocity SO maps. The orange image, white contours, and green contours have the same meaning as those in Figure 1. (a) The total low-velocity map with $V_{\text{off}} \sim -3$ to 3 km s^{-1} . (b) The blueshifted ($V_{\text{off}} \sim -3$ to 0 km s^{-1}) and redshifted ($V_{\text{off}} \sim 0$ to 3 km s^{-1}) low-velocity maps separately. (c) The blueshifted ($V_{\text{off}} \sim -10$ to -3 km s^{-1}) and redshifted ($V_{\text{off}} \sim 3$ to 10 km s^{-1}) high-velocity maps separately. The star marks the protostar position. The white curves in panel (a) guide the readers for the shell structure. The contour levels start at 3σ with a step of 2σ , where $\sigma = 4.5 \text{ mJy beam}^{-1} \text{ km s}^{-1}$ in panels (a) and (c), and $3 \text{ mJy beam}^{-1} \text{ km s}^{-1}$ in panel (b).

The physical properties (e.g., radius, rotation velocity, expansion velocity, and specific angular momentum) of the shell in the north, where the shell is detected at a higher signal-to-noise ratio and better resolved, can be estimated from the elliptical PV structures seen in the PV diagrams cut across the jet axis in Figures 7(a)–(g). As can be seen, the elliptical PV structures can be roughly described by the green ellipses in the figures. Since the elliptical PV structures are not well defined, we only used an eye-fitting to roughly obtain the green ellipses, which are required to pass through the emission in the shells as much as possible. From these green ellipses, the radius of the shell is given by the maximum position offset from the jet axis, the rotation velocity is given by the velocity at the maximum position offset with respect to the velocity centroid of the ellipse, and the expansion velocity is given by the velocity at the zero position offset with respect to the velocity centroid of the ellipse. The specific angular momentum is then derived by

multiplying the rotation velocity with the radius. These physical quantities of the shell are shown in Figure 8, with their uncertainties described in the caption. Since the inclination angle of the outflow is small, no correction is needed for the inclination effect. As expected, the shell becomes wider with the distance (Figure 8(a)). Interestingly, the rotation velocity is roughly the same as the expansion velocity in the shell inside the atmosphere, but becomes much smaller than the expansion velocity in the shell outside the atmosphere (Figure 8(b)). The specific angular momentum in the shell is roughly constant at $\sim 40 \text{ au km s}^{-1}$ within $\sim 50 \text{ au}$ of the central source, and then decreases to $\sim 25 \text{ au km s}^{-1}$ at $\sim 80 \text{ au}$ (Figure 8(c)). This decrease in the specific angular momentum is uncertain because the rotation velocity cannot be estimated accurately outside the atmosphere due to the poorly identified elliptical PV structure.

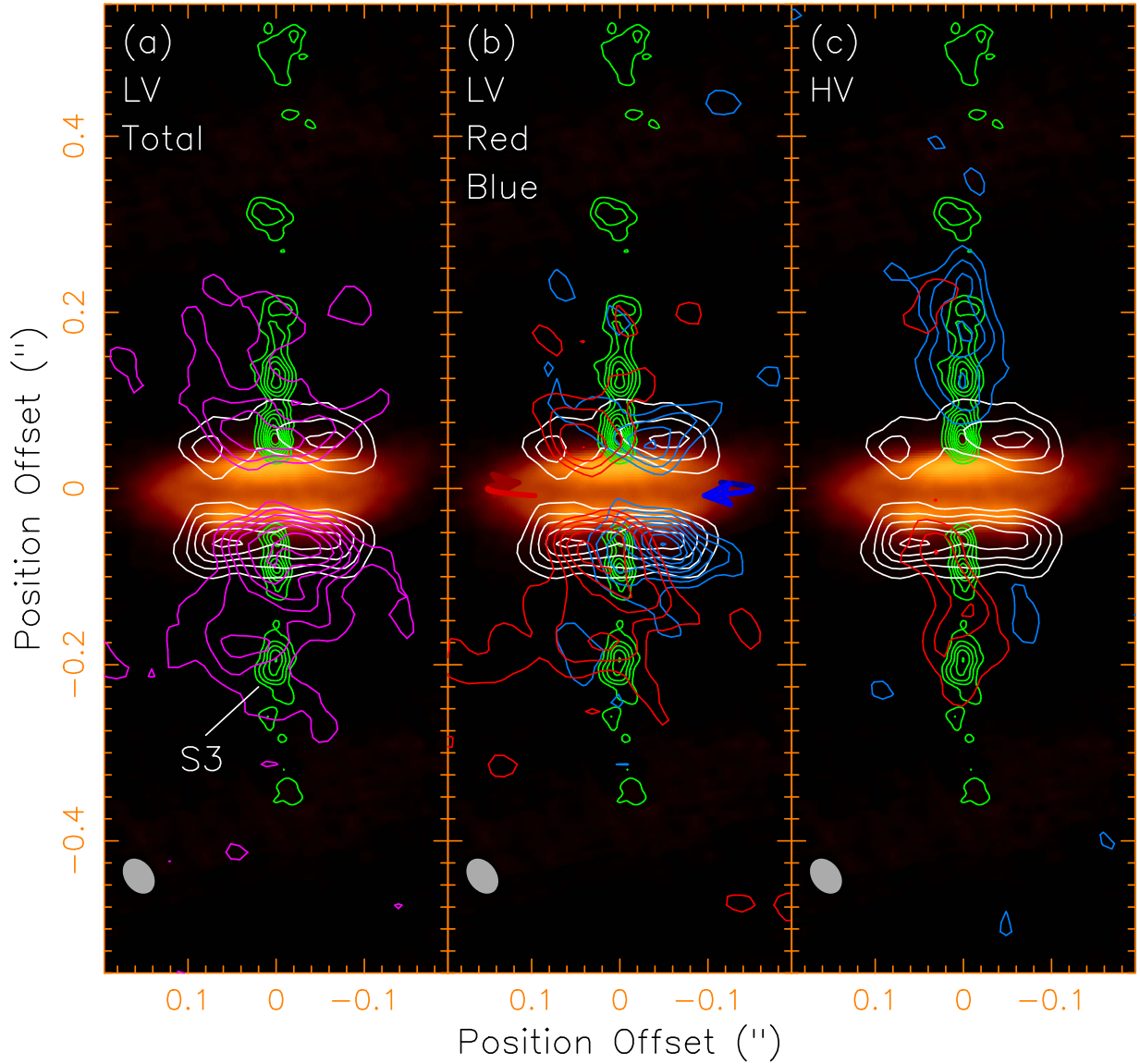


Figure 4. Low-velocity and high-velocity SO_2 maps. The orange image, white contours, and green contours have the same meaning as those in Figure 1. (a) The total low-velocity map, with $V_{\text{off}} \sim -3$ to 3 km s^{-1} . (b) The blueshifted ($V_{\text{off}} \sim -3$ to 0.0 km s^{-1}) and redshifted ($V_{\text{off}} \sim 0$ to 3 km s^{-1}) low-velocity maps separately. The red and blue arrows show the rotation of the disk. (c) The blueshifted ($V_{\text{off}} \sim -7.9$ to -3 km s^{-1}) and redshifted ($V_{\text{off}} \sim 3$ to 6.5 km s^{-1}) high-velocity maps separately. The star marks the protostar position. The white curves in panel (a) guide the readers for the shell structure. The contour levels start at 3σ with a step of 2σ , where $\sigma = 1.5 \text{ mJy beam}^{-1} \text{ km s}^{-1}$ in panel (a), and $1.1 \text{ mJy beam}^{-1} \text{ km s}^{-1}$ in panels (b) and (c).

3.4. Physical Condition in the Disk Atmosphere and Shell

With 12 SO_2 lines detected, we can construct a population diagram (Goldsmith & Langer 1999) to estimate the rotational temperature and the column density of the molecule in the disk atmosphere, the wide-angle outflow shell, and the collimated jet. It is a diagram that plots the column density per statistical weight in the upper energy state in the optically thin limit, N_u^{thin}/g_u , versus the upper energy level E_u of the lines. Here $N_u^{\text{thin}} = (8\pi k\nu^2/hc^3 A_{ul})W$, where the integrated line intensity $W = \int T_B dv$ with T_B being the mean brightness temperature.

The integrated line intensity of each transition can be measured for the SO_2 emission in the south, where the emission is detected at a higher signal-to-noise ratio. The resulting population diagram is shown in Figure 9. Fitting the data points with $E_u > 70 \text{ K}$, we estimate a rotational temperature of $81 \pm 20 \text{ K}$ and a column density of $8.2 \pm 2.0 \times 10^{15} \text{ cm}^{-2}$. Notice that the data points with $E_u < 70 \text{ K}$ are not used for the

fitting because their emissions are only barely detected, with their intensity slightly over 3σ . These estimated values are mainly for the disk atmosphere and the outflow shell, because SO_2 emission is mainly detected there.

The SO emission traces mainly the outflow shell and the collimated jet. The excitation temperature is unknown. Along the jet axis, the emission has a peak brightness temperature of $\sim 150 \text{ K}$ and a mean integrated line intensity of 700 K km s^{-1} . Thus, we assume a temperature of $\sim 200\text{--}300 \text{ K}$ in the collimated jet, which is consistent with the temperature range discussed in Podio et al. (2015). The column density of SO there is then estimated to be $\sim (1.5\text{--}1.8) \times 10^{16} \text{ cm}^{-2}$. In the shell, the mean integrated line intensity is $\sim 400 \text{ K km s}^{-1}$. The excitation temperature can be assumed to be $\sim 100 \text{ K}$, which is an approximation to that derived above in SO_2 for the disk atmosphere and the outflow shell. Thus, the SO column density is estimated to be $\sim 6 \times 10^{15} \text{ cm}^{-2}$ in the outflow shell.

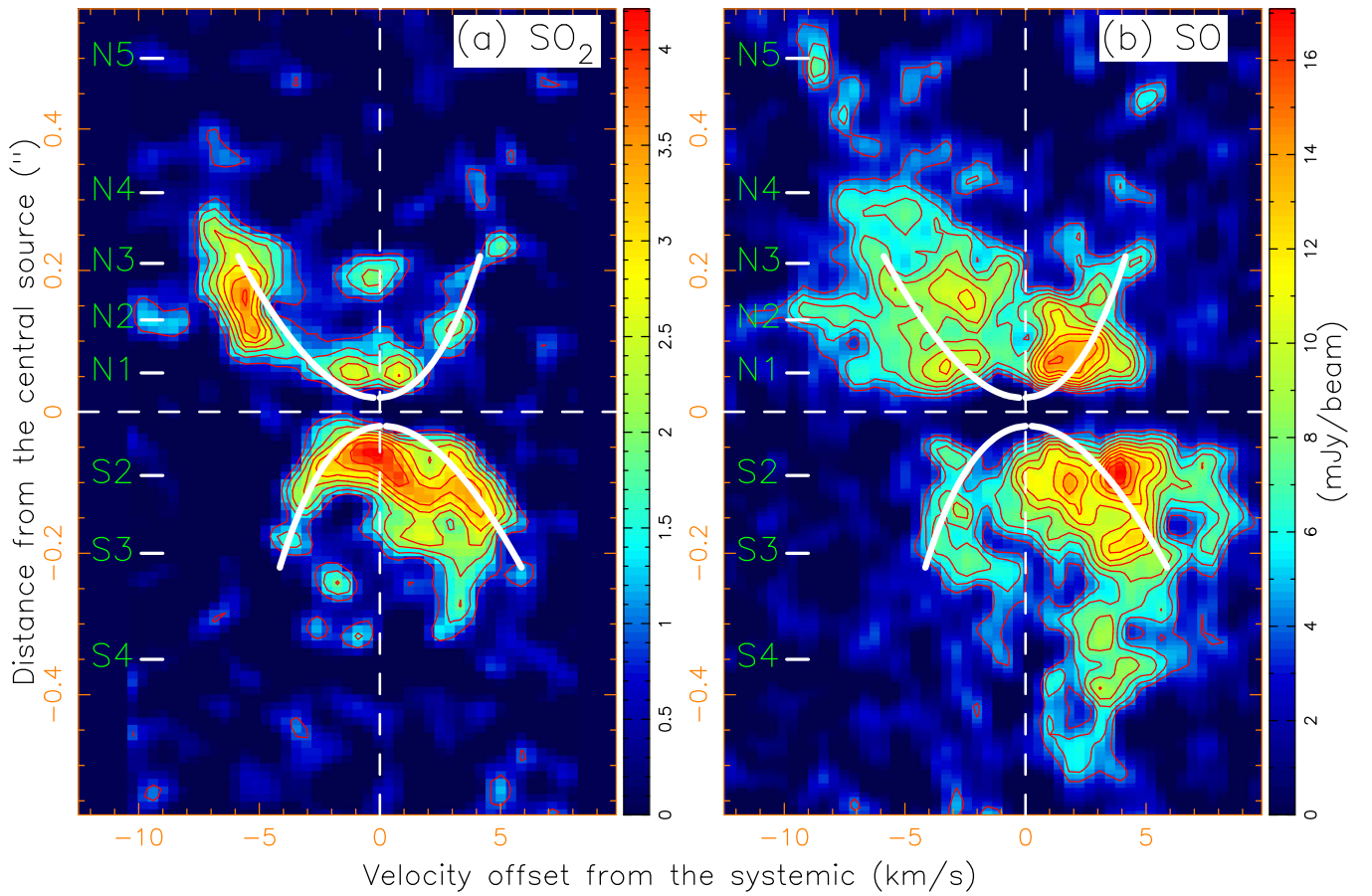


Figure 5. Position–velocity diagrams of the SO (contours) and SO₂ (color image) emissions cut along the jet axis. The contours start at 3σ with a step of 1σ , where $\sigma = 1.4$ mJy beam^{−1}. The white curves guide the readers for the parabolic PV structure of the outflow shell.

The abundances of SO and SO₂ have been estimated before at lower resolution by comparing their column density to that derived from the CO $J = 3-2$ emission (see Table 3 in Podio et al. 2015) and thus can be used here to derive the mean H₂ column density. With a SO abundance of $(1-10) \times 10^{-7}$, the mean H₂ column density is estimated to be $(6-60) \times 10^{21}$ cm^{−2} in the SO shell. With a SO₂ abundance of $(5-12) \times 10^{-7}$, the mean H₂ column density is estimated to be $(5-12) \times 10^{21}$ cm^{−2} in the SO₂ shell. Given that the thickness of the shell is $\lesssim 50$ au, the mean H₂ density is $\gtrsim (4-40) \times 10^6$ cm^{−3} in the SO shell, and $(3-8) \times 10^6$ cm^{−3} in the SO₂ shell. As can be seen, the SO shell could have a higher mean H₂ density than that in the SO₂ shell.

4. Discussion

4.1. Disk wind?

In star formation, one important topic is to search for a low-velocity disk wind that can carry away the disk angular momentum, allowing the disk material to accrete. Previously, a rotating outflow was detected in CB 26 in CO $J = 2-1$ emission and was argued to trace a disk wind launched from a radius of ~ 30 au in the disk (Launhardt et al. 2009). Later, a rotating outflow was also detected in Orion BN/KL Source I in SiO maser, appearing to be a disk wind launched from a radius of ~ 20 au in the disk (Matthews et al. 2010). In recent follow-up observations of the same object, a rotating outflow was also detected further out in Si¹⁸O, and argued to trace a disk wind launched from a radius of > 10 au (Hirota et al. 2017). Recently, another rotating outflow was detected in TMC1A

in CO $J = 2-1$, and also argued to trace a disk wind launched from a radius of > 5 au in the disk (Bjerkeli et al. 2016). Another example is HH 30, where a rotating CO ($J = 2-1$) shell is observed to surround one side of the bipolar optical jet (F. Louvet et al. 2018, in preparation).

In HH 112, we can search for a disk wind emerging from the well-resolved disk. As discussed later, the wind’s source can be on the disk 2–3 au from the protostar. At this radius, the density and temperature on the disk surface (at one scale height) are estimated to be $\sim (2-4) \times 10^{12}$ cm^{−3} and 770–1050 K, respectively, based on the disk model in Lee et al. (2017b). Thus, our SO and SO₂ lines, with a critical density of $\sim 10^7$ cm^{−3}, are better tracers of a disk wind than the CO $J = 2-1$ line, which has a critical density of $\sim 10^4$. However, note that, since only charged particles are directly coupled to the magnetic field, neither CO and SO/SO₂ can be directly accelerated by a magnetic field; they must be coupled to magnetically accelerated charged particles through collisions.

Recently, a compact outflow has been detected in HH 212 at ~ 52 au ($0''.13$) resolution, extending out from the disk (Tabone et al. 2017). It is rotating and thus may trace a disk wind. Now at ~ 16 au ($0''.04$) resolution, the compact outflow is found to consist of two distinct components: a wide-angle outflow shell and a collimated jet. The collimated jet is aligned with the SiO jet and thus likely traces the shock interactions along the jet axis. Interestingly, the outflow shell lies within the large-scale molecular outflow detected in C³⁴S (Codella et al. 2014) and HCO⁺ (Lee et al. 2017c), and is thus not the rotating envelope material pushed away by the underlying wind or jet (see

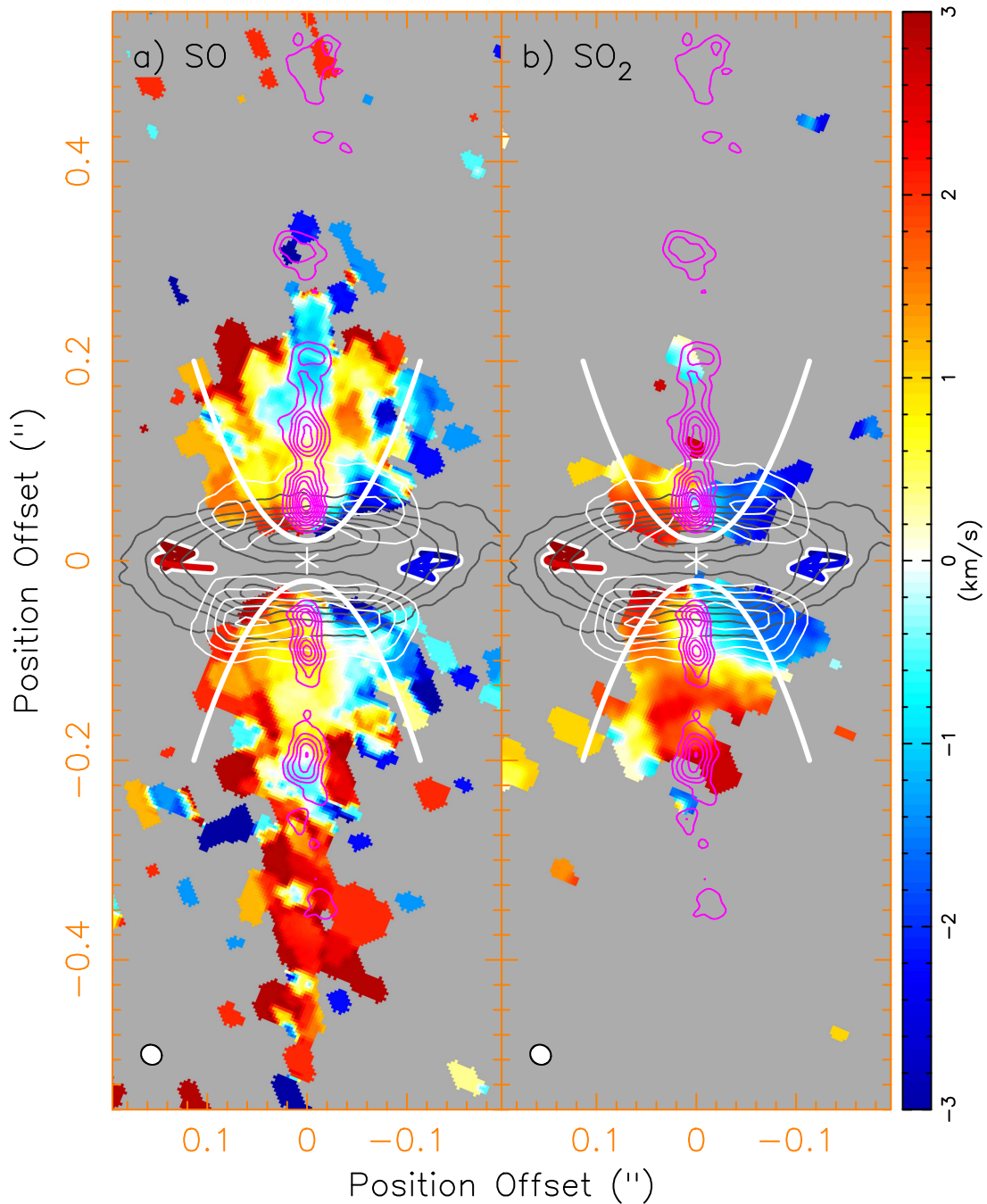


Figure 6. Intensity weighted velocity (first moment) maps of the SO and SO₂ emission at low velocities, plotted together with the maps of the dusty disk (gray contours), disk atmosphere (white contours), and SiO jet (magenta contours). The red and blue arrows show the rotation of the disk.

Figure 10 for various components). Moreover, it is rotating and seen extending out from the inner disk at a radius of <20 au within the centrifugal barrier (Lee et al. 2017c), and thus may trace a disk wind coming out from there. The specific angular momentum is roughly constant at ~ 40 au km s⁻¹ within ~ 50 au of the central source. This specific angular momentum corresponds to that at ~ 7.2 au in the disk, where the rotation velocity is ~ 5.5 km s⁻¹, assuming a central mass of $0.25 M_{\odot}$ (Lee et al. 2017c). It decreases to ~ 25 au km s⁻¹ at a distance of ~ 80 au. This decrease in specific angular momentum could be inconsistent with that expected for a disk wind; however, further observations are needed to confirm this. On the other hand, it is also possible that the SO/SO₂ outflow shell is the

disk/atmosphere material pushed up and out by a wind launched at the innermost disk, e.g., by a wide-angle radial wind component surrounding the fast jet as in the X-wind model.

The shell kinematics could be used to differentiate the above two origins of the outflow shell. If the shell traces the disk wind itself, the velocity vectors are expected to be parallel to the shell structure. If the shell traces the disk or atmosphere material pushed away by a wide-angle radial wind, then the velocity vectors in the shell are expected to be radially directed. For simplicity, the shell here can be assumed to roughly have a parabolic structure with $z = CR^2 + 0''.02$ in the cylindrical coordinate system and $C \sim 14$ arcsec⁻¹ (as indicated by the

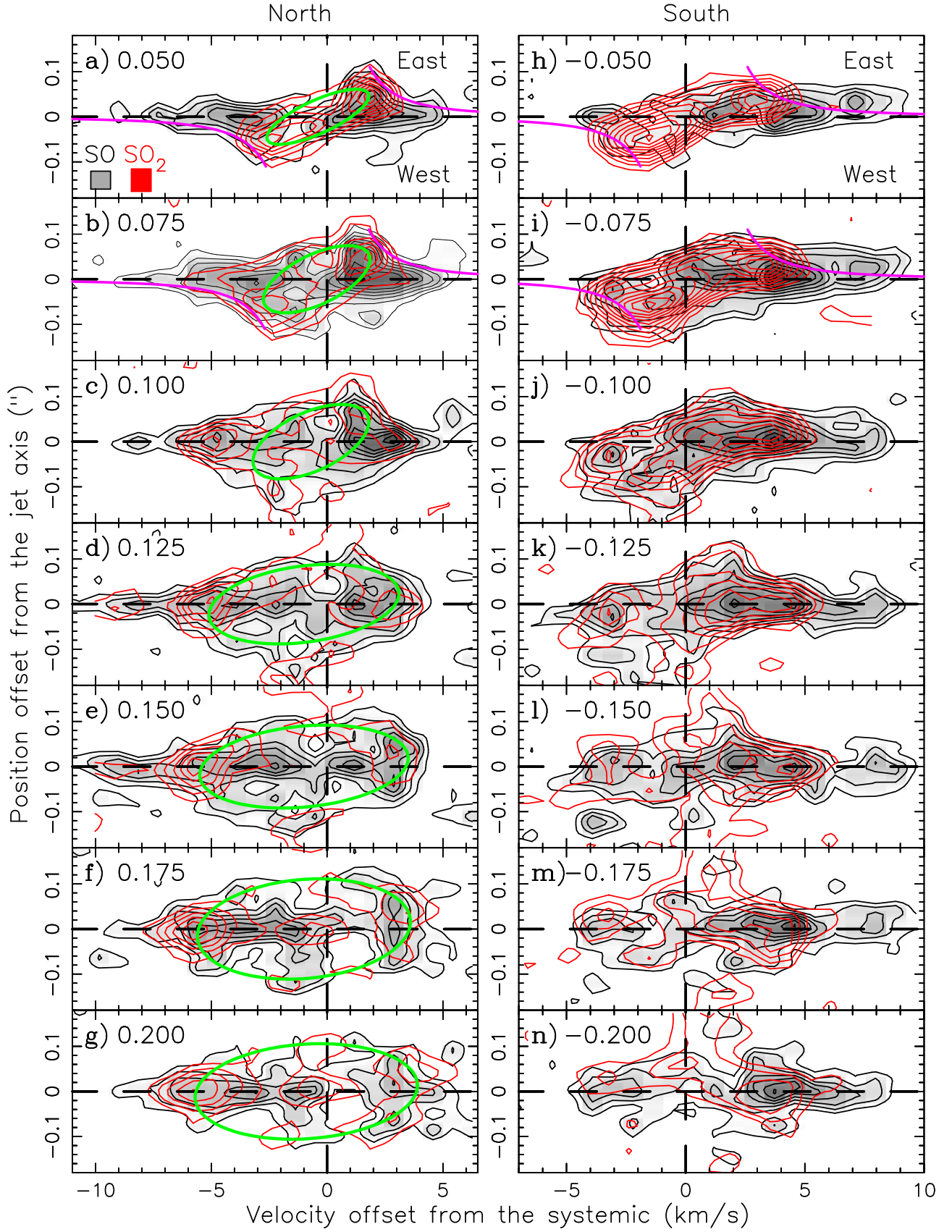


Figure 7. PV diagrams of the SO and SO₂ emissions across the jet axis at increasing distance from the central source. Left column is for the north and right is for the south. The number in the upper left corner indicates the distance from the central source along the jet axis. The gray image with black contours is for SO emission. The contours start at 3σ with a step of 2σ , where $\sigma = 1.1 \times 10^{-3} \text{ Jy beam}^{-1}$. Red contours are for SO₂ emission. The contours start at 3σ with a step of 1.5σ , where $\sigma = 3.4 \times 10^{-4} \text{ Jy beam}^{-1}$. The green ellipses guide the readers for the elliptical PV structures of the shell. The magenta curves show the Keplerian rotation velocity profile due to the central protostar (Lee et al. 2017c). In the upper left panel, the rectangles in the lower left corner show the resolutions of the cuts in SO and SO₂.

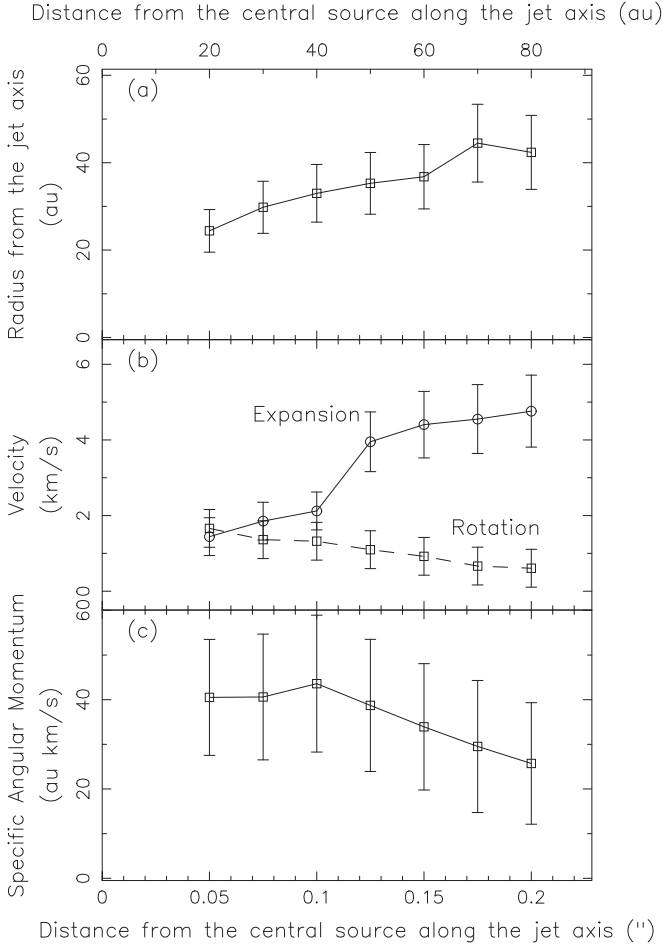


Figure 8. Radius, expansion velocity, rotation velocity, and specific angular momentum of the shell in the north at different distances from the central source above the disk midplane. They are derived from the elliptical PV structures seen in Figures 7(a)–(g). The radius is assumed to have an uncertainty of 20%. The expansion velocity is assumed to have an uncertainty of 20% or 0.5 km s^{-1} (about a half of the channel width), whichever is larger. The rotation velocity is small and thus assumed to have an uncertainty of 0.5 km s^{-1} (i.e., about half of the channel width). The resulting uncertainty in the specific angular momentum is about 30%–50%.

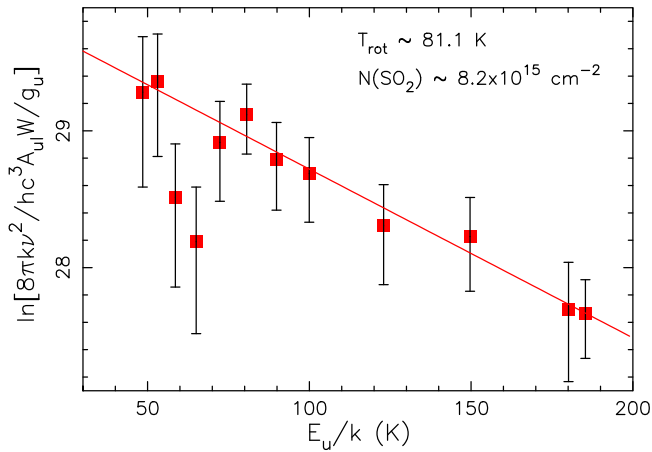


Figure 9. Population diagram for SO_2 , derived from the total intensity map for the disk atmosphere and outflow shell in the south. The error bars show the uncertainties in our measurements, which are assumed to scale inversely with the integrated line intensity, with 25% of the data values for the highest integrated line intensity and 50% for the lowest integrated line intensity. The solid line is a linear fit to the data with $E_u > 70 \text{ K}$.

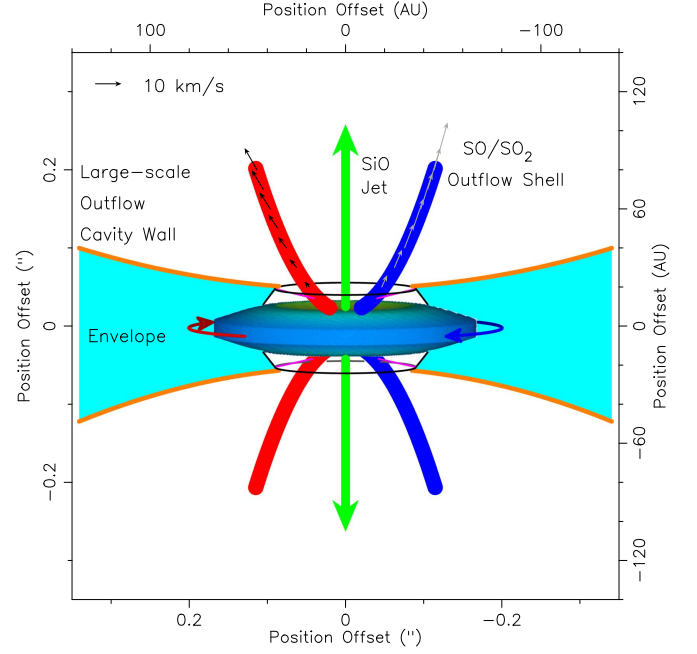


Figure 10. Schematic diagram showing the wide-opening SO/SO_2 outflow shell in connection to the SiO jet, and other components (e.g., infalling-rotating envelope, dusty disk, disk atmosphere, and large-scale outflow cavity walls) presented in Figure 9(b) of Lee et al. (2017c). Black arrows show the velocity vectors in the radially expanding shell model, while gray arrows show the velocity vectors in the material moving along the shell model.

white curves in Figure 6). If the shell material is moving along the shell, then we have $v_R = v_0 R$ and $v_z = 2v_0 z$ in the cylindrical coordinate system. If the shell material is radially expanding, then we have $v_R = v_0 R$ and $v_z = v_0 z$ (Lee et al. 2000). Figure 11 shows the model PV structures of these two models at an inclination angle of $\sim 4^\circ$, in comparison to the observed PV structures. The solid curves are from the radially expanding shell model with $v_0 \sim 42 \text{ km s}^{-1} \text{ arcsec}^{-1}$ and the dotted curves are from the material moving along the shell model with $v_0 \sim 45 \text{ km s}^{-1} \text{ arcsec}^{-1}$. The velocity vectors and magnitudes in these two models are shown in Figure 10, with the black arrows for the former and gray arrows for the latter. As can be seen, both model PV structures can match the observed PV structure reasonably well. Therefore, unfortunately, we cannot determine which model is better based on the kinematics here in HH 12. Having said that, it is unclear whether a disk wind can have an expansion speed that increases with the distance from the disk and at the same time a specific angular momentum that decreases with distance. For a shell accelerated by an underlying wide-angle radial wind, it is reasonable to have an expansion velocity increasing with the distance (Shu et al. 1991; Lee et al. 2000), because the disk atmosphere has a density decreasing with height. Whether the specific angular momentum can naturally decrease with distance in this scenario is uncertain. In addition, the shell in the north is seen connecting to knot N4 further north, which is likely also affected by it (see Figure 3).

Another question we can ask is the following: does the wide-angle wind component of an X-wind, if it exists, have enough momentum to drive the outflow shell? The mass of the shell can be roughly estimated from the mean H_2 column density derived from the SO emission in Section 3.4. Thus, the total mass of the shell within $\sim 0''.2$ of the central source in the north and south is $M_s = 1.4 m_{\text{H}_2} N_{\text{H}_2} A \sim (0.4\text{--}4) \times 10^{-4} M_\odot$, where A is the area of

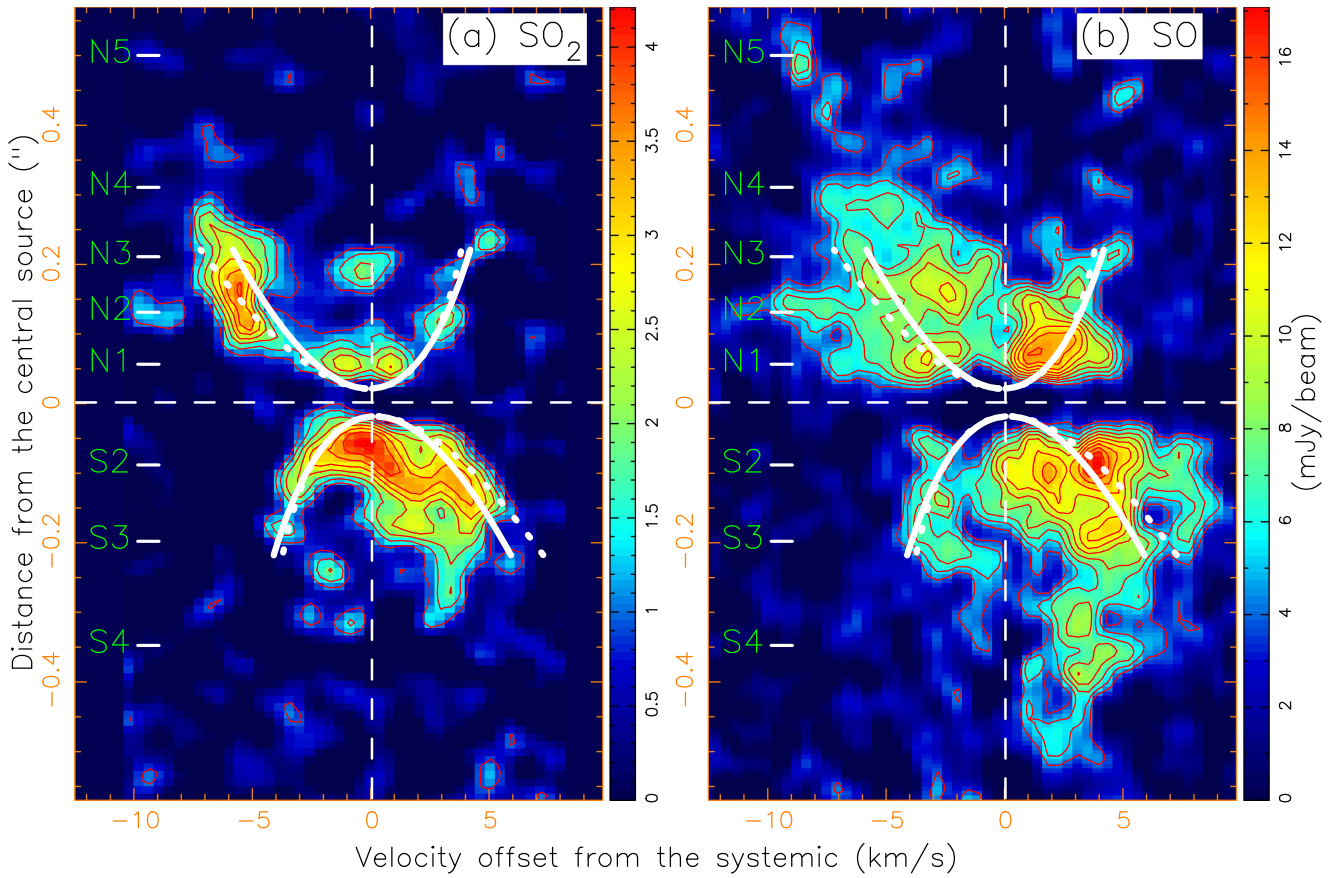


Figure 11. Same as Figure 5, but with two model PV structures added. The solid curves are for the radial expanding shell model with $v_0 \sim 42 \text{ km s}^{-1} \text{ arcsec}^{-1}$ and the dotted curves are for the material moving along the shell model with $v_0 \sim 45 \text{ km s}^{-1} \text{ arcsec}^{-1}$.

the shell. Assuming a mean expansion velocity of $\sim 5 \text{ km s}^{-1}$ in the shell, the momentum is then $(0.2\text{--}2) \times 10^{-3} M_\odot \text{ km s}^{-1}$. In the X-wind model, the wide-angle wind component could have a mass-loss rate and a velocity similar to those of the jet component (Shu et al. 1995). The jet component was found to have a mass-loss rate of $\sim 10^{-6} M_\odot \text{ yr}^{-1}$ and a velocity of $\sim 100 \text{ km s}^{-1}$ (Lee et al. 2015). According to our simple radially expanding model for the shell, the shell has a dynamical age of $1/v_0$ or ~ 45 years, indicating that the shell could have been driven for that long by an underlying wind. Thus, the wide-angle wind component can, in principle, provide an accumulated momentum of $\sim 4.5 \times 10^{-3} M_\odot \text{ km s}^{-1}$, enough to drive the shell.

One more question to ask is the following: why is there only one shell? In the case of a radial expanding shell, the shell has a dynamical age much younger than the age of HH 12. Since the jet is episodic, the inner wind that drives the shell should also be episodic. Since the semi-periodic spacing between two bow shocks in the jet is $\sim 3''$ (Lee et al. 2007), the period for the major ejection of the jet/wind is ~ 50 years and thus slightly longer than the dynamical age of the shell. Therefore, it is possible that the shell was produced recently and the earlier shells are lost in the outflow cavity probably because the density becomes too low to excite the SO and SO_2 lines. Or as suggested in Tabone et al. (2017), the shell traces an onion-like shell in the disk wind coming out from the disk around the SiO jet (see their Figure 3), but the part further away from the central source is lost in the cavity.

Independent of the exact mechanism for producing the outflow shell, if it is really rotating with a specific angular

momentum of $\sim 40 \text{ au km s}^{-1}$, it is likely coming from the disk at a relatively large radius of at least several astronomical units. If the outflow is indeed an MHD disk wind from the disk, then using Equation (4) in Anderson et al. (2003), and an outflow velocity of $5\text{--}10 \text{ km s}^{-1}$, the launching radius is estimated to be $2\text{--}3 \text{ au}$. The specific angular momentum is much larger than the mean value for the SiO jet ($\sim 10 \text{ au km s}^{-1}$), indicating that the outflow shell is not simply the jet angular momentum and is much larger than the mean value for the SiO jet (\sim material that is swept into a shell). One may argue that the shell material may come from the infalling protostellar envelope that extends all the way to less than several astronomical units above and below the disk. However, the large-scale outflow cavity wall, which presumably marks the inner boundary of the envelope, is located well outside of the outflow shell (as indicated in the cartoon of Figure 10). Furthermore, in the case of a much more evolved T Tauri star HH 30, there is little evidence for a large-scale envelope, and yet a rotating, expanding shell is still observed surrounding the jet (F. Louvet et al. 2018, in preparation), indicating that an envelope is not needed for producing such a structure. This leaves the material coming directly from the disk as the most likely material for the outflow shell.

The key question is whether that disk material in the outflow shell is launched from the several astronomical unit radius by some mechanism internal to the local disk, such as through magnetocentrifugal acceleration or magnetic pressure gradient, or by some external agents, such as interaction with a wide-angle wind surrounding the SiO jet. Indeed, the two mechanisms are not mutually exclusive: outflow launched from the several

astronomical unit radius is expected to interact with the wide-angle wind interior to it, if such a wind exists. In any case, the rotating outflow shell carries away angular momentum from the disk, most likely from the several astronomical unit radius, which is in contrast with the rotating SiO jet driven from the ~ 0.05 au radius.

4.2. Formation of SO and SO₂

Previous observations of HH 212 at an angular resolution of $\sim 0''.5$ have shown that the SO and SO₂ abundances in the outflow are very high, up to $\sim 10^{-6}$ (Podio et al. 2015). Now at higher resolution, the outflow is resolved into a small-scale wide-opening outflow shell and a collimated jet. The high SO and SO₂ abundances in the collimated jet could be due to violent (internal) shocks in the jet. The origin of high abundances in the wide-angle outflow shell is uncertain. If the shell traces a disk wind launched from the disk, then the high abundances could be due to the thermal sublimation of icy mantles near the source and the gradual heating by ambipolar diffusion during MHD acceleration (Panoglou et al. 2012). If the shell is the disk/atmosphere material pushed away by an inner wind, then the high abundances could be due to shock interactions with the inner wind.

As for the disk, Podio et al. (2015) have found a high SO abundance of 10^{-8} – 10^{-7} . Our observations also show high SO and SO₂ column densities (see Section 3.4) and thus high SO and SO₂ abundances there in the disk atmosphere. These high abundances in the disk atmosphere could be due to the accretion shocks already observed in HH 212 by Lee et al. (2017a), radiation heating by the central protostar, or shock interactions with an inner wind.


5. Conclusions

We have mapped the central 400 au region in the HH 212 protostellar system in SO and SO₂, with the Atacama Large Millimeter/submillimeter Array at ~ 16 au resolution. We have resolved the compact outflow near the central source into a wide-opening rotating outflow shell with a width of ~ 100 au and a collimated jet. The collimated jet is aligned with the SiO jet and thus likely traces the shock interactions along the jet axis. The wide-opening outflow shell is seen around the base of the collimated SiO jet, extending out from the inner disk. It is not only expanding away from the center, but also rotating around the jet axis. The specific angular momentum of the outflow shell is ~ 40 au km s⁻¹. Simple modeling suggests that this rotating outflow shell can trace either a disk wind or disk material pushed away by an unseen inner wind. We also resolve the disk atmosphere traced by the two S-bearing molecules, confirming the Keplerian rotation there.

We thank the anonymous referee for useful comments. This paper makes use of the following ALMA data: ADS/JAO. ALMA# 2015.1.00024.S. ALMA is a partnership of ESO (representing its member states), NSF (USA), and NINS (Japan), together with NRC (Canada), MoST and ASIAA (Taiwan), and KASI (Republic of Korea), in cooperation with the Republic of Chile. The Joint ALMA Observatory is operated by ESO, AUI/NRAO, and NAOJ. C.-F.L. acknowledges grants from the Ministry of Science and Technology of Taiwan (MoST 104-2119-M-001-015-MY3) and the Academia Sinica (Career Development Award). Z.Y.L. is supported in

part by NASA NNX14AB38G and NSF AST-1313083 and 1716259. This research was carried out in part at the Jet Propulsion Laboratory, California Institute of Technology, under a contract with the National Aeronautics and Space Administration.

ORCID iDs

Chin-Fei Lee  <https://orcid.org/0000-0002-3024-5864>
 Claudio Codella  <https://orcid.org/0000-0003-1514-3074>
 Hsien Shang  <https://orcid.org/0000-0001-8385-9838>
 Neal J. Turner  <https://orcid.org/0000-0001-8292-1943>
 Qizhou Zhang  <https://orcid.org/0000-0003-2384-6589>

References

- Agra-Amboage, V., Dougados, C., Cabrit, S., & Reunanen, J. 2011, *A&A*, **532**, A59
 Anderson, J. M., Li, Z.-Y., Krasnopolsky, R., & Blandford, R. D. 2003, *ApJL*, **590**, L107
 Balbus, S. A., & Hawley, J. F. 2006, *ApJ*, **652**, 1020
 Bjerkeli, P., van der Wiel, M. H. D., Harsono, D., Ramsey, J. P., & Jørgensen, J. K. 2016, *Natur*, **540**, 406
 Charnley, S. B. 1997, *ApJ*, **481**, 396
 Claussen, M. J., Marvel, K. B., Wootten, A., & Wilking, B. A. 1998, *ApJL*, **507**, L79
 Codella, C., Bachiller, R., Benedettini, M., et al. 2005, *MNRAS*, **361**, 244
 Codella, C., Cabrit, S., Gueth, F., et al. 2014, *A&A*, **568**, L5
 Dutrey, A., Wakelam, V., Boehler, Y., et al. 2011, *A&A*, **535**, A104
 Fuente, A., Cernicharo, J., Agúndez, M., et al. 2010, *A&A*, **524**, A19
 Goldsmith, P. F., & Langer, W. D. 1999, *ApJ*, **517**, 209
 Greenhill, L. J., Goddi, C., Chandler, C. J., Matthews, L. D., & Humphreys, E. M. L. 2013, *ApJL*, **770**, L32
 Guillet, V., Pineau des Forêts, G., & Jones, A. P. 2011, *A&A*, **527**, 123
 Hatchell, J., Thompson, M. A., Millar, T. J., & MacDonald, G. H. 1998, *A&A*, **338**, 713
 Hirota, T., Machida, M. N., Matsushita, Y., et al. 2017, *NatAs*, **1**, 0146
 Konigl, A., & Pudritz, R. E. 2000, in *Protostars and Plane IV*, ed. V. Mannings, A. P. Boss, & S. S. Russell (Tucson, AZ: Univ. Arizona Press), 759
 Launhardt, R., Pavlyuchenkov, Y., Gueth, F., et al. 2009, *A&A*, **494**, 147
 Lee, C.-F., Hasegawa, T. I., Hirano, N., et al. 2010, *ApJ*, **713**, 731
 Lee, C.-F., Hirano, N., Zhang, Q., et al. 2015, *ApJ*, **805**, 186
 Lee, C.-F., Ho, P. T. P., Hirano, N., et al. 2007, *ApJ*, **659**, 499
 Lee, C.-F., Ho, P. T. P., Li, Z.-Y., et al. 2017a, *NatAs*, **1**, 0152
 Lee, C.-F., Hwang, H.-C., & Li, Z.-Y. 2016, *ApJ*, **826**, 213
 Lee, C.-F., Li, Z.-Y., Ho, P. T. P., et al. 2017b, *SciA*, **3**, e1602935
 Lee, C.-F., Li, Z.-Y., Ho, P. T. P., et al. 2017c, *ApJ*, **843**, 27
 Lee, C.-F., Mundy, L. G., Reipurth, B., Ostriker, E. C., & Stone, J. M. 2000, *ApJ*, **542**, 925
 Leurini, S., Codella, C., Cabrit, S., et al. 2016, *A&A*, **595**, L4
 Matthews, L. D., Greenhill, L. J., Goddi, C., et al. 2010, *ApJ*, **708**, 80
 Panoglou, D., Cabrit, S., Pineau Des Forêts, G., et al. 2012, *A&A*, **538**, A2
 Pineau des Forêts, G., Roueff, E., Schilke, P., & Flower, D. R. 1993, *MNRAS*, **262**, 915
 Podio, L., Codella, C., Gueth, F., et al. 2015, *A&A*, **581**, A85
 Podio, L., Lefloch, B., Ceccarelli, C., Codella, C., & Bachiller, R. 2014, *A&A*, **565**, A64
 Sakai, N., Oya, Y., Higuchi, A. E., et al. 2017, *MNRAS*, **467**, L76
 Sakai, N., Oya, Y., López-Sepulcre, A., et al. 2016, *MNRAS*, **820**, L34
 Sakai, N., Oya, Y., Sakai, T., et al. 2014a, *ApJL*, **791**, L38
 Sakai, N., Sakai, T., Hirota, T., et al. 2014b, *Natur*, **507**, 78
 Shu, F. H., Najita, J., Ostriker, E. C., & Shang, H. 1995, *ApJL*, **455**, L155
 Shu, F. H., Ruden, S. P., Lada, C. J., & Lizano, S. 1991, *ApJL*, **370**, L31
 Tabone, B., Cabrit, S., Bianchi, E., et al. 2017, *A&A*, **607**, L6
 Tieftrunk, A., Pineau des Forêts, G., Schilke, P., & Walmsley, C. M. 1994, *A&A*, **289**, 579
 van Dishoeck, E. F., & Blake, G. A. 1998, *ARA&A*, **36**, 317
 Wakelam, V., Caselli, P., Ceccarelli, C., Herbst, E., & Castets, A. 2004, *A&A*, **422**, 159
 Wiseman, J., Wootten, A., Zinnecker, H., & McCaughrean, M. 2001, *ApJL*, **550**, L87
 Zinnecker, H., Bastien, P., Arcoragi, J.-P., & Yorke, H. W. 1992, *A&A*, **265**, 726